1 # A water-repellent low dimensional fluorous

2 # perovskite as interfacial coating for 20% efficient

3 # solar cells.

4 *Kyung Taek Cho, [1,‡] Yi Zhang [1,‡,†], Simonetta Orlandi [2], Marco Cavazzini [2], Iwan Zimmermann [1],*

5 *Andreas Lesch [3], Nouar Tabet [4], Gianluca Pozzi, [2*] Giulia Grancini [1*] and Mohammad Khaja*

6 *Nazeeruddin [1*]*

7

8 [1] Group for Molecular Engineering of Functional Materials, Ecole Polytechnique Fédérale

9 Lausanne Valais Wallis, CH-1951 Sion, Switzerland

10 [2] Istituto di Scienze e Tecnologie Molecolari del CNR, ISTM-CNR, via Golgi, 19, I-20133

11 Milano, Italy

12 [3] LEPA, Ecole Polytechnique Fédérale Lausanne Valais Wallis, Sion CH-1951, Switzerland

13 [4] Qatar Environment and Energy Research Institute, Hamad Bin Khalifa University (HBKU),

14 Qatar Foundation, Doha, 5825, Qatar

15

16

17 ABSTRACT. Hybrid perovskite solar cells have been capturing an enormous research interest in

18 the energy sector due to their extraordinary performances and ease of fabrication. However, low

19 device lifetime, mainly due to material and device degradation upon water exposure, challenges

20 their near-future commercialization. Here, we synthesized a new fluorous organic cation used as

21 organic spacer to form a low dimensional perovskite (LDP) with an enhanced water-resistant

22 character. The LDP is integrated with 3D perovskite absorbers in the form of $MA_{0.9}FA_{0.1}PbI_3$ (FA

23 $= NH_2CH=NH_2^+$, $MA=CH_3NH_3^+$) and $Cs_{0.1}FA_{0.74}MA_{0.13}PbI_{2.48}Br_{0.39.}$ In both cases a LDP layer self-

24 assembles as a thin capping layer on the top of the 3D bulk, making the perovskite surface

25 hydrophobic. Our easy and robust approach, validated for different perovskite compositions, limits

26 the interface deterioration in perovskite solar cells yielding to > 20% power conversion efficient

27 solar cells with improved stability, especially pronounced in the first hours of functioning under

28 environmental conditions. As a consequence, single and multi-junction perovskite devices, such

29 as tandem solar cells, can benefit from the use of the water-proof stabilization here demonstrated,

30 a concept which can be further expanded in the perovskite optoelectronic industry beyond

31 photovoltaics.

32 KEYWORDS. Perovskite solar cells, Fluorinated organic salt, passivation, low dimensional

33 perovskite, 2D/3D perovskite.

34

35 Organic and inorganic hybrid perovskites have revealed a burgeoning technology with

36 demonstrated power conversion efficiency (PCE) beyond 22%,[1,2] setting the promise for a near-

37 future alternative for efficient and low-cost solar energy production.[3,4] However, the poor device

38   stability, due to degradation upon water exposure, still impedes the lunch in the market.[5,6] In

39   presence of moisture, hydrolysis of the perovskite happens, triggered by the hygroscopic nature of

40   the material. The degradation is mediated by the formation of a perovskite hydrate (i.e.

41   monohydrate $CH_3NH_3PbI_3 \cdot H_2O$, followed by the formation of dihydrate $(CH_3NH_3)_4PbI_6 \cdot 2H_2O)$,

42   which lately decomposes back into precursors (i.e. PbI_2)[5,6]. In parallel, prolonged exposure to water

43   and high temperature induces the deterioration of the solar cell electrodes due to reaction with the

44   byproducts (i.e. HI) of the perovskite decomposition. This leads to the diffusion of the organic

45   HTM into the perovskite active layer with the subsequent degradation of the device interface, a

46   phenomenon that results in as a drop in the photovoltaics performances upon few hours of

47   operation.[7] Different solutions, including compositionally and structural engineering of the

48   perovskite itself,[8,9] interface functionalization with protective layers[10] or substitution of organic

49   HTM with more stable carbon electrode into a HTM-free device architecture have been shown.[11,12]

50   Despite some incremental improvements, superior costs and device complexity, and lower

51   performances come along, still questioning the validity of these approaches. More recently, low

52   dimensional perovskites (LDP), such as arranging into the *Ruddlesden–Popper* phase, have been

53   proposed as one of stable alternatives to the common mixed halide three dimensional (3D)

54   perovskites.[14–20] LDP can be conceptually obtained by slicing a generic ABX_3, (A = MA, or FA;

55   B= Pb; X =Cl, Br or I) 3D perovskite network across the inorganic planes, spaced by large organic

56   cations, typically protonated primary amines with an extended linear organic portion. This results

57   in layered structures of the general formula $R_2(A)_{n-1}B_nX_{3n+1}$, where R is the additional large cation

58   (e.g. *n*-butyl ammonium or phenethylammonium) and *n* represents the number of inorganic slabs

59   spaced by the large organic cations, R, barrier layers.[16,19] The highly oriented structure and dense

60   packing of the $R_2(A)_{n-1}B_nX_{3n+1}$ materials have demonstrate to reduce the possibility of direct contact

61 with water, thus preventing the formation of the initial hydrate phase. [5,6] This in turns reduces the

62 grain boundaries and prevents direct contact of adventitious water with the perovskite, ultimately

63 boosting the stability. When incorporated as active layer in solar cells, LDP bring about improved

64 stability, at the expense, however, of limited PCE due to their contrasting optoelectronic properties,

65 such as high exciton binding energy, high band gap and limited charge transport, not ideal for

66 photovoltaic applications.[12,21–24] However, if combined together with 3D perovskites in a 2D/3D

67 hybrid, a synergic action can be designed to boost efficiency and stability. [12,25–27] In particular,

68 2D/3D composites, obtained by blending standard bulky organic cations (as R component) with

69 the precursor of the 3D perovskite, have been recently embodied in solar cells to push device

70 performances and stability. [26-28] By blending, the bulk organic cations can penetrate in the

71 perovskite matrix and either passivate the trap site at the grain boundaries or at the interface with

72 the 3D perovskites. As a consequence, improved thermal stability compared to 3D perovskites has

73 been shown due to the reduced defect density and self-healing effects. [26,28] However, surface

74 properties and water repellent character have been neither targeted nor elucidated yet. In this work,

75 we push forward the concept of engineering 2D/3D composites, aiming to create a LDP water-

76 repellent sheath, containing a saturated highly fluorinated (fluorous) organic cation designed *ad*

77 *hoc*, on the top of the 3D perovskite bulk. In addition, we evaluate the effect of the fluorous

78 perovskite by incorporating the cation in two alternative ways: a) by direct blending of the LDP-

79 and 3D perovskite precursors; b) by engineering a controlled *in situ* layer by layer approach which

80 enables the construction of a clean 3D/2D interface, as pictured in Figure 1a. More in details, we

81 incorporated the LDP in two different 3D perovskite compositions, $MA_{0.9}FA_{0.1}PbI_3$ (MFPI) and

82 $Cs_{0.1}FA_{0.74}MA_{0.13}PbI_{2.48}Br_{0.39}$ (CFMPIB). In the first case, the fluorous cation was added to the

83 MFPI perovskite precursors; in the second case the cation was deposited on top of preformed

84   CFMPIB through a passivation layer by layer approach. In both cases, a thin layer of fluorous LDP

85   self-assembles on the top surface of the 3D bulk, forming a water-proof sheath. The presence of

86   the top LDP layer also improves the device open circuit voltage (V_{OC}), possibly due to reduced

87   interfacial back charge recombination. In parallel, the perovskite/HTM interface, which is known

88   to be the gate for water penetration initiating the interface deterioration and device degradation,

89   becomes less sensitive to humidity and more robust to ion migration processes. As a result, the

90   device degradation that usually occurs in the first hours under operation, is hampered. Importantly,

91   for both perovskite bulk compositions here considered, efficient devices have been developed

92   delivering PCE of more than 20% with little hysteresis and enhanced open circuit voltage (V_{OC}).

93   Fluorous compounds contain highly fluorinated saturated molecular fragments C_nF_{2n+1} ($n \geq 4$)

94   and show distinct properties, such as a dual hydrophobic/lipophobic character and the tendency to

95   self-organize and packing into highly stable and ordered assemblies, compared to their fully

96   hydrocarbon-, mono/polyfluorinated- or trifluoromethylated analogues. These properties can be

97   transferred to advanced materials built around them.[29] Capitalizing on this knowledge, we

98   envisaged the use of properly designed fluorous ammonium cations to modulate the dimensionality

99   perovskite materials and template the formation of LDP structures. Indeed, because of their shape

100   and large size, much beyond the one of standard MA and FA cations which fit in the voids of the

101   3D perovskite structure, these cations might act as effective spacers between PbX_6 octahedra

102   layers.[16,18,30] The robustness of fluorous LDP compared to standard LDP might be enhanced due

103   to the hydrophobic and solvophobic character of the perfluoroalkyl residues. Based on these

104   premises, we synthesized the fluorous cation $(CF_3)_3CO(CH_2)_3NH_3^+$ in the form of its iodide salt

105   (named A43 in the following, synthetic details in the Supplementary Information). Its structure is

106   depicted in Figure 1b. Single crystals of LDP have been grown from a solution of A43, PbI_2 and

107   MAI (2:2:1 molar ratio) in aqueous 48% HI (see Supplementary Information for details). Two

108   defined structures, arranging into *Ruddlesden–Popper* phase of $(A43)_2PbI_4$ and $(A43)_2MAPb_2I_7$,

109   as derived by X-ray diffraction (XRD) measurement, have been obtained (see Figure 1c,

110   crystallographic information in Table S1). In the case of $(A43)_2PbI_4$ perovskite structure, bilayers

111   of bulky A43 cations of 20.65 Å in length intercalate in between monolayers of PbI_6 octahedra.

112   For $(A43)_2MAPb_2I_7$, bilayers of A43 cations intercalate in between bilayers of PbI_6 octahedra in

113   which MA cations are confined, the distance between with MA cations in two contiguous inorganic

114   slabs being 26.64 Å (see Figure 1c).

115   As mentioned above, we explored two different strategies in order to prepare 2D/3D composites

116   based on A43. The first approach consisted in mixing A43 with standard perovskite precursors in

117   solution to grow thin film, as depicted in top scheme of Figure 1a. Thus, a solution containing A43

118   and PbI_2 (molar ratio 2:1; 1.15 M in A43) is directly blended with PbI_2, MAI and FAI in DMSO

119   (molar ratio 1:0.9:0.1; 1.15 M in PbI_2) at different volume ratio, in order to achieve a final content

120   of A43 of 6, 10, and 20%. A single step spin coating is used to deposit the mixed solution (see

121   Methods for details) followed by standard antisolvent dropping method to obtain a smooth and

122   uniform thin perovskite film. Figure 2a shows the absorption spectra of the films of MFPI/ 6%

123   A43, while Figure S3 shows the absorption spectra for MFPI with increasing amount of A43. The

124   absorption edge falls at around 780 nm independently from %A43, similarly to the pristine MFPI

125   (= 0% A43).[13,31,32] It is fair to point out, however, that upon adding 20% A43, the band edge

126   experiences a tiny blue-shift and a remarkable shoulder at 550 nm appears (see Figure S3). These

127   observations suggest that upon adding A43, except for the case of 20% A43, where a different

128   feature in the absorption profile is observed, the perovskite film retains the optical properties (i.e.

129   band gap) of the MFPI perovskite. Figure 2b reports the X-ray diffraction (XRD) patterns of the

130   MFPI films containing different A43 %. On top of the reflections indicative of the formation of a

131   3D perovskite structure which adopts a tetragonal phase at room temperature, [13,32] the XRD patterns

132   indicate a different relative intensity of the doublets at 26 – 28.5°. Upon the addition of A43, the

133   peak at 28.5° increases with respect to the peak at 26°(see Figure S4 for a magnified spectra),

134   which indicates a preferential oriented growth, possibly induced by the presence of the fluorous

135   compounds. Note that, in this case, no clear evidence of LDP reflections, usually appearing at

136   angles < 10°, are observable. This can be due to the very small amount of LDP phase formed, with

137   a non-detectable signal.

138   As a second different approach (bottom scheme in Figure 1a), we incorporated A43 in CFMPIB

139   using a controlled *in situ* layer by layer passivation method. This is obtained by coating the top of

140   the CFMPIB triple cation mixed perovskite film with a solution of A43 in isopropanol using a

141   dynamical spin coating approach. In the pristine CFMPIB perovskite film, lead in excess interacts

142   with A43, inducing the formation of a thin LDP layer on the top surface of the 3D perovskite bulk.

143   Figure 2a shows the absorption spectra of pure CFMPIB and CFMPIB treated with A43

144   (CFMPIB/A43). CFMPIB shows a blue shifted band edge, due to the incorporation of Cs, with

145   respect to MFPI, but no appreciable difference are observable in the absorption spectra of samples

146   treated with A43. However, for the latter XRD spectra confirm the presence of a thin layer of

147   deposited LDP on top of CFMPIB (Figure 2c). Indeed, the XRD pattern of CFMPIB/A43 shows

148   the distinct features at 4.3° and 8.4°, indicative of the existence of a LDP as may be inferred by

149   comparison with the XRD pattern of the pure LDP perovskite thin film in the form of $(A43)_2PbI_4$,

150   which shows the same reflection pattern (Figure 2c and Figure S5) with main peak at 4.3°. In

151   addition, the 3D phase is also present, as revealed by the XRD peak at 14.1°, indicating that the

152   growth of the LDP top layer does not alter the structure of the 3D CFMPIB perovskite underneath.

153   To assess the presence of the LDP layer, we measured the photoluminescence (PL) spectra of

154   the perovskites containing A43. First, it is worth mentioning that PL measurements both at bottom

155   side and top surface of perovskite films reveal a main peak close to the band edge (around 770

156   nm), matching with the band gap emission for the 3D perovskites. This was observed for both

157   MFPI- and CFMPIB-based materials. In case of MFPI, standard PL measurements do not reveal

158   any other features upon the addition of any considered amount of A43 (see Figure 3a). However,

159   a closer inspection, monitoring the PL signal only from the top surface layer using a confocal

160   micro-PL setup in epi-configuration mode (which mainly probes the signal from the top surface),

161   reveals an additional PL peak for the 6 – 10 – 20 % A43 doped MFPI films at around 570 nm

162   (Figure 3b). The peak grows in intensity with the amount of A43, without shifting in energy.

163   Notably, this emission is not observed measuring on the back side of the film (Figure 3a). The

164   results indicate that the A43 modulates the nature of the perovskite material inducing the formation

165   of a fluorous LDP phase retained on the surface of the MFPI perovskite bulk. This fluorous

166   perovskite emits at 570 nm, indicative of a higher energy band gap material with respect to MFPI.

167   This also agrees with the shoulder manifested for the 20%A43 sample in the absorption spectrum

168   at 550 nm (Figure S3). The assignment of the PL peak at 570 nm to a LDP phase is further

169   confirmed upon measuring the emission from the sub-millimetre-size LDP single crystals shown

170   in Figure 1c. The emission of the $(A43)_2MAPb_2I_7$ perovskite crystal falls at around 570 nm, shown

171   as dashed line of Figure 3b, fairly matching with the peak registered from the fluorous LDP surface

172   layer. This spectral match provides evidence that the incorporation of the A43 % induces the

173   formation of a fluorous LDP perovskite self-assembled on the top surface of the MFPI, maintaining

174   the structural integrity of both LDP and 3D phases. This is made possible by the intrinsic self-

175   organization tendency of the fluorous cations and their orthogonal properties with respect to

176   organic substances.[25] Notably, the emission peak at 570 nm provides an upper esteem of the LDP

177   band gap, in agreement with values reported in literature for non-fluorinated LDP arranging into a

178   *Ruddlesden–Popper* phase.[16] Likewise, for CFMPIB/A43 material built by the layer-by-layer

179   approach, a thin layer of LDP at the top surface of the 3D CFMPIB perovskite was observed by

180   comparison of PL emission spectra from bottom and top side (Figure 3c). Exciting from the bottom

181   side at 400 nm wavelength laser, which only interrogates the first 80-100 nm thickness, the PL

182   spectrum resembles the one of the standard CFMPIB, peaking at 760 nm, signature of band to

183   band charge recombination. On the other side, exciting from the top surface, the PL spectrum is

184   more structured, with a secondary main peak at 540 nm. This result can be rationalized considering

185   the formation of a LDP, $(A43)_2PbI_4$, at the top surface. A secondary peak around 570 nm is also

186   visible, possibly due to a minor contribution from the emission of the $(A43)_2MAPb_2I_7$. Thus, PL

187   measurements unambiguously prove the presence of a top LDP layer in both MFPI- and CFMPIB-

188   based materials, despite the different methods used to introduce A43.

189   In the case of the MFPI/A43 sample, the LDP induces an enhanced directionality, evidenced by

190   the XRD results, which also manifests as an oriented morphology visible from the top surface

191   analysis of the scanning electron microscopy (SEM) images (Figure 4a, b and Figure S6). A rod-

192   like morphology with remarkable orientation is also visible on the macroscopic scale. On the other

193   hand, the presence of a LDP passivating layer on top of the CFMPIB surface does not change

194   dramatically the morphology of perovskite films, as shown in Figure 4c and d. The main rough

195   surface of the CFMPIB film is maintained and the additional layer covers the whole surface of the

196   pristine perovskite film that assumes the appearance of a rock floor.

197   Notably, the presence of the fluorous cation modifies the water affinity degree of the perovskite

198   surface. Figure 4e compares the images of water contact angle measured for the LDP-covered

199   surface. In this case, a significant increase (>50%) of the contact angle, from 55° to close to 90 °

200   (MFPI/A43) and higher (CFMPIB/A43), is observed, thus providing compelling evidence that the

201   fluorous ammonium cation improves the water-proof character of the perovskite surface. Although

202   small fluorinated ammonium cations used as dopants in perovskite materials have already proven

203   a slight enhancement of the water contact angle (i.e. from 44° to 49°),[33] the improvement caused

204   by the presence of A43 is remarkably higher making the perovskite surface hydrophobic. This can

205   be hardly explained on the base of a simple average effect as that induced by a dopant, but it fits

206   well with the formation of a stable fluorinated hydrophobic surface. To further evaluate the

207   properties of our fluorous LDP in terms of moisture resistance, we conducted moisture stability

208   tests comparing the bare 3D perovskite films to the ones engineered with the LDP layer by

209   incorporating the A43 cations. In particular, we registered the XRD patterns (see Figure S7) and

210   any changes in the position and intensity of the XRD peaks comparing fresh films and films stored

211   for 3 days under high humid air (50 $\pm$ 5%) circulation system. According to the XRD results

212   (shown in Figure S7a), pure 3D MFPI perovskite undergoes complete decomposition much faster

213   than the MFPI/A43 perovskite containing 6% A43. This is evident from monitoring the ratio of

214   the peak at 12.5° (marker of PbI_2, as a result from the degradation of the 3D perovskite) to the

215   peak at 14° (marker of the 110 diffraction from the tetragonal phase of the 3D perovskite). The

216   ratio grows enormously for the pure 3D film with respect to the one processed with 6% A43,

217   indicating a fast degradation for the pure 3D perovskite, which, on the contrary, the top LDP layer

218   is able to retard. A similar beneficial effect in slowing down material degradation is also observed

219   comparing the CFMPIB- and CFMPIB/A43 perovskite films (shown in Figure S7b). After 3 days

220   in high humid air, the pristine CFMPIB perovskite decomposes into PbI_2, which is not observed

10

221 in the case of CFMPIB/A43, further proving the ability of the passivating fluorous LDP layer to

222 block water penetration and the ensuing degradation of the 3D perovskite bulk.

223 Cross-sectional SEM images of solar cells based on MFPI/6%A43 and CFMPIB/A43 with the

224 same device configuration (FTO/blocking TiO_2/meso-TiO_2/3D perovskite layer/spiro-

225 OMeTAD/gold) are displayed in Figure 4f. The current (J)–voltage (V) characteristics of the cells

226 fabricated with MFPI/6% A43 and CFMPIB/A43 compared to the controller samples with no LDP

227 are shown in Figure 5a, b and Figure S8. Device parameters are listed in the Figures insets. The

228 MFPI perovskite devices (0 % A43) deliver average PCE of 18%, in line with literature.[13] Upon

229 adding A43 up to 10%, an improvement of the device performances is observed. Note that using

230 a larger amount of A43 (20%), on the other side, the performance drops again, possibly due to the

231 exceeding amount of LDP perovskite in the hybrid material (see Figure S8). A champion device

232 showing PCE beyond 20% is obtained for the optimal 6% A43 value. Interestingly, the layered

233 CFMPIB/A43 solar cells also shows improved performances, delivering a PCE of 20% to the best

234 and outperforming the benchmark CFMPIB device. In both cases, a net improvement of the device

235 open circuit voltage (V_{OC}) is observed, possibly due to reduced recombination at the LDP interface.

236 Further studies are ongoing to specifically monitor the interface processes. The improvement in

237 the PCE in both cases broadens the importance of our results and enables us to further validate the

238 impact of our LDP- coating. The incident photon-to-current conversion efficiency spectra for

239 MFPI containing 6% A43 and integrated photocurrent are reported in Figure S9 (see also device

240 statistics in Figure S10 and in Table S2). In addition, to monitor the effect of the interfacial

241 functionalization with fluorous LDP on device operation, we measured the J-V characteristic of

242 solar cells based on MFPI containing 6% A43 scanning the voltage at different speed rate. The J-

243 V characteristic (Figure S11) is not affected by the scan speed, which suggest that the LDP

244   interlayer has a beneficial effect on reducing the ion movement which usually happens in

245   perovskite solar cell. Device performances with few hundreds hours under operation are measured

246   comparing solar cells fabricated using MFPI with and without the addition of 6% A43 in inert gas

247   system, respectively (see Figure 5c). For comparison, the behaviour of cells fabricated with LDP

248   thin film in the form of $(A43)_2PbI_4$ is also examined (see Figure S12). A remarkable long term

249   stability is recorded for pure LDP based solar cells (Figure 5c), while the MFPI/6% A43 device

250   shows a better stability with respect to standard MFPI, especially in the initial 100 hours operation.

251   In standard $MAPbI_3$ and MFPI perovskite devices, an initial drop in stability tests is usually

252   observed and commonly ascribed to the degradation of the device interface, mainly due to the

253   inter-diffusion of HTM and top electrode inside the perovskite layer and to ion movement and

254   charge accumulation at the perovskite/HTM interface.[7,34–38] Here, the enhanced initial stability in

255   the performance of the LDP-MFPI shows that the vertically segregated fluorous LDP solar cell is

256   unaffected by this phenomenon, showing a zero-loss in the performance in the first 200 hours. On

257   the other side, for the CFMPIB/A43 solar cells, a less pronounced improvement in the solar cell

258   stability, already pretty high for the bare CFMPIB, is observed (see Figure S13). This analysis

259   enables us to conclude that the fluorous LDP within MFPI perovskite is able to prevent the first

260   step of solar cell degradation, blocking water penetration and retarding the interface degradation,

261   a remarkable step forward in the perovskite solar cell research.

262   In conclusion, we developed a new fluorous cation to realize a water-proof sheath consisting of

263   a self-assembled hydrophobic fluorous LDP on top of a MFPI as well as CFMPIB perovskites.

264   The vertical segregation of the LDP on top of the 3D perovskites keeps intact the excellent

265   structural and optoelectronic properties of the 3D bulk, reducing the water induced degradation,

266   while improving its interface with the HTM. As a result, the device performances do not drop in

267   the first hundred hour of operation, and the device Voc is enhanced. Remarkably, the enhanced

268   stability does not compromise the device performances, but it rather improves them, leading to

269   water-proof 20% efficient solar cell. A thin layer coating approach using the fluorous LDP is also

270   demonstrated, showing enhanced performances, beyond 20% kept intact over time, a record for

271   perovskite solar cells employing LDP. We believe our approach through the hydrophobic fluorous

272   cation widens the perspectives of perovskite material in the energy sector, opening up many further

273   technological developments of low-dimensional perovskite system, as well charting the way for

274   the design and implementation of stable multi-dimensional hybrid perovskites beyond the solely

275   photovoltaic industry.

276   **Methods**

277   **Synthesis of A43.** The fluorous ammonium salts was prepared according to a procedure

278   summarized in Figure S1 (Supporting Information). Reactions were monitored by thin layer

279   chromatography (TLC) that was conducted on plates precoated with silica gel Si 60-F254 (Merck,

280   Germany). Column chromatography was conducted by using silica gel Si 60, 230–400 mesh,

281   0.040–0.063 mm (Merck, Darmstadt, Germany). 1H and 13C NMR spectra were recorded on a

282   Bruker Avance 400 (400 and 100.6 MHz, respectively); chemical shifts are indicated in parts per

283   million downfield from SiMe4, using the residual proton (CHCl3 = 7.26 ppm) and carbon (CDCl3

284   = 77.0 ppm) solvent resonances as the internal reference. 19F NMR spectra were recorded on a

285   Bruker AC 300 spectrometer (282MHz) using CFCl3 (0.00 ppm) as the external reference.

286   Coupling constant values J are given in Hz. Accurate mass analyses were carried by a VG

287   Autospec M246 (Fisons) spectrometer having a EBE geometry, equipped with EI source.

288   **Device Preparation.** Chemically etched FTO glass (Nippon Sheet Glass) was cleaned with

289   detergent solution, acetone, and isopropanol. To form a 20 to 25 nm thick TiO_2 blocking layer,

290   diluted titanium diisopropoxide bis(acetylacetonate) (TAA) solution (Sigma-Aldrich) in ethanol

291   (0.2 ml of TAA in 6 ml of anhydrous ethanol) was sprayed at 450 °C. A 200-nm mesoporous TiO_2

292   was coated on the substrate by spin coating at a speed of 2000 rpm for 10 s with a ramp-up of 1000

293    $rpm \cdot s^{-1}$ from a commercially available TiO_2 paste (Dyesol-30NRD) in ethanol; the weight ratio of

294   TiO_2 paste to ethanol is 9:1. After spin coating, the substrate was immediately dried on a hotplate

295   at 80 °C, and the substrates were then sintered at 500 °C for 20 min before the deposition of the

296   perovskite layer. A DMSO solution of 3D perovskite precursors, 1.15 M in PbI_2, 1.035 M in MAI

297   and 0.115 M in FAI (solution A), and a second DMSO solution, 1.15 M in fluorous salt and 0.575

298   M in PbI_2 (solution B) were prepared. Variable volumes of the two solutions were mixed (e.g. 94

299   mL of A and 6 mL of B for 6%A43) to give final solutions containing the desired amount of

300   fluorous salt. These last solutions were then spin-coated on the substrates in a two-step procedure

301   at 1000 rpm for 10 s and 5000 rpm for 30 s, respectively. During the second step, 100 μL of

302   chlorobenzene was deposited in the last 10 s at 5000 rpm. Perovskite films were annealed at 100

303   °C for 50 min. For triple cation perovskite solar cells, the lead excess $(FAPbI_3)_{0.85}(MAPbBr_3)_{0.15}$

304   precursor solution was prepared by mixing FAI (1.1 M), PbI_2 (1.15 M), MABr (0.2 M) and

305    $PbBr_2$ (0.2 M) in a mixed solvent of DMF : DMSO = 4 : 1 (volume ratio). Another 1.15 M solution

306   of $CsPbI_3$ was also prepared in DMF : DMSO (with the same volume ratio). For triple cation mixed

307   perovskite solution, $(FAPbI_3)_{0.85}(MAPbBr_3)_{0.15}$ and $CsPbI_3$ solutions were mixed in 10 vol% ratio.

308   The solution was then spin-coated at 1000 rpm for 10 s and continuously at 4000 rpm for 30 s in

309   a nitrogen glove box. After entering the second step, 100 µl of anhydrous trifluorotoluene was

310   poured 15 seconds before the completion of the process. Films were then annealed at 100 °C for

311   60 min. For forming an additional 2D perovskite film on top of this perovskite film, cooled

312   substrates were treated with a A43 isopropanol solution. 100 μl of A43 solution (6 mg ml^{-1}) were

313   spin-coated on the as-prepared perovskite films at 4000 rpm, which is similar to the anti-solvent

314   dropping method and heated additionally for 5 min. [36] The HTM solution was prepared by

315   dissolving 91 mg of Spiro-OMeTAD (Merck) with additives in 1 mL of chlorobenzene. As

316   additives, 21 μL of Li-bis(trifluoromethanesulfonyl) imide from the stock solution (520 mg in 1

317   mL of acetonitrile), 16 μL of FK209 [tris(2-(1H-pyrazol-1-yl)-4-tert-butylpyridine)-cobalt(III)

318   tris(bis (trifluoromethylsulfonyl)imide) (375 mg in 1 mL of acetonitrile) and 36 μL of 4-

319   tertbutylpyridine were added. The HTM layer was formed by spin-coating the solution at 4000

320   rpm for 20 s, and followed by the deposition of the 70 nm thick Au electrode by a thermal

321   evaporation. All the preparative work to deposit perovskite and Spiro-OMeTAD was done inside

322   a glove box filled with nitrogen to minimize the influence of moisture.

323   **Device characterization.** Current–voltage characteristics were recorded by applying an external

324   potential bias to the cell while recording the generated photocurrent with with a potentiostat

325   (Keithley 2604). The light source was a VeraSol LED solar simulator (Newport) producing 1 Sun

326   AM 1.5 (1,000 W m^{-2}) sunlight. The light intensity was calibrated with a NREL-certified KG5-

327   filtered Si reference diode. The solar cells were masked with a metal aperture of 0.16 cm^2 to define

328   the active area. Hysteresis curves were routinely recorded. Full solar cells were fabricated

329   alongside the half-devices analyzed during this study in order to perform the fundamental

330   characterization on high efficient devices. For stability measurements, solar Cells were placed in

331   a sealed cell holder with a glass cover that was flushed with a flow of argon of 30 mL/min. The

332   holder was therefore exempt of water and oxygen, avoiding the need of sealing and improving the

333   reproducibility. J/V curves were characterized by an electronic system using 22 bits delta-sigma

334 analogic to digital converter. For J/V curves measurement, a scan rate of 25 mV/s with a step of 5

335 mV was used, maintaining the temperature of the holder at 35 °C while the temperature of the cells

336 reached around 45 °C. Between each measurement the cells were maintained at the maximum

337 power point using a MPPT algorithm under 100mW/cm^2. A reference Si-photodiode was placed

338 in the holder to verify the stability of the light.

339 **Absorption and Photoluminescence Measurements.** Absorption spectra were registered with

340 a UV-VIS-IR spectrophotometer (*PerkinElmer Instrument*). Photoluminescence (PL)

341 Measurements: CW PL experiments were performed using a laser diode at 532nm coupled within

342 an optical microscope (Renishaw microscope, equipped with 5x, 20x, 50x and 100x short and long

343 working distance microscope objectives) used to focus the excitation light and collect it in a back

344 scattering epi-configuration confocal mode. The sample was mounted on a translation stage of a

345 Leica microscope. The system was calibrated against the 520.5 cm^{-1} line of an internal silicon

346 wafer. Data were averaged over 10 accumulations in order to maximize the signal to noise ratio.

347 The measurements were conducted at room temperature on encapsulated samples (encapsulated

348 inside N_2 glovebox) using the 100x long working distance objective (spot size of about 330 nm).

349 To prevent sample degradation or thermal effects the laser power intensity was kept relatively low

350 with an excitation density of around 1μJ/cm^2 and the light exposure time per measurement of 0.1

351 seconds. No visible degradation signs were observed. Sample were encapsulated with a thin quartz

352 window.

353 **Scanning electron microscope (SEM)/Energy-dispersive X-ray (EDX).** Film morphology

354 was investigated by using a high-resolution scanning electron microscope (Merlin, Zeiss) equipped

355 with a GEMINI II column and a Schottky Field Emission gun. Images were acquired with an In-

356   Lens Secondary Electron Detector. EDX maps were recorded using a Quantax spectrometer from

357   Bruker.

358   **X-Ray Diffraction (XRD) characterization.** The X-ray diffractogram of perovskite- (on glass

359   + device) was recorded using a Bruker D8 Advance machine.

360
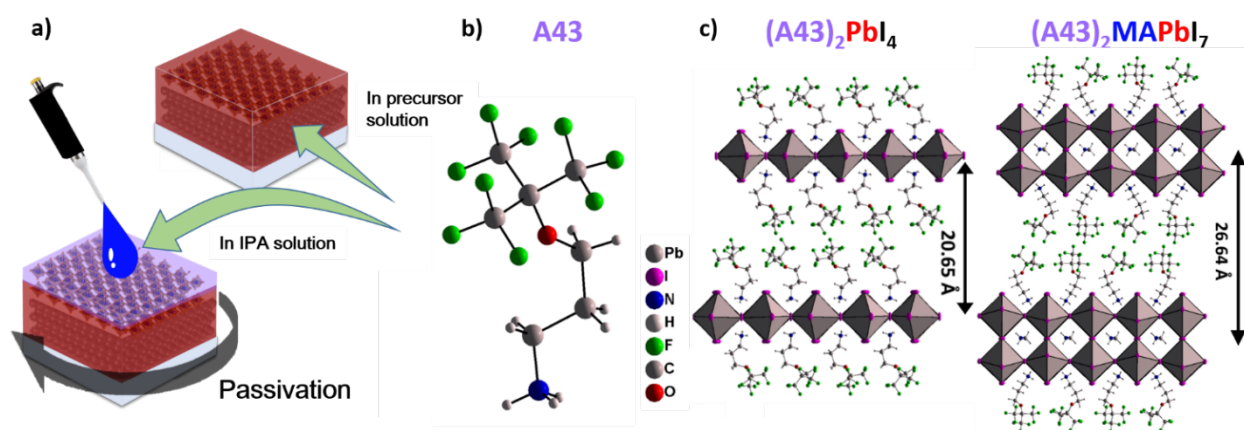
361
362

363   **Figure 1.** a) Schematic diagram showing the methods used to incorporate fluorous LDP on top of

364   the 3D perovskites, in the precursor solution for MFPI or as layer by layer on top of the CFMPIB,

365   respectively. b) Structure of the fluorous organic cation. c) Crystal structure of the fluorous LDP

366   arranging into $(A43)_2PbI_4$ or $(A43)_2MAPb_2I_7$.

367

368
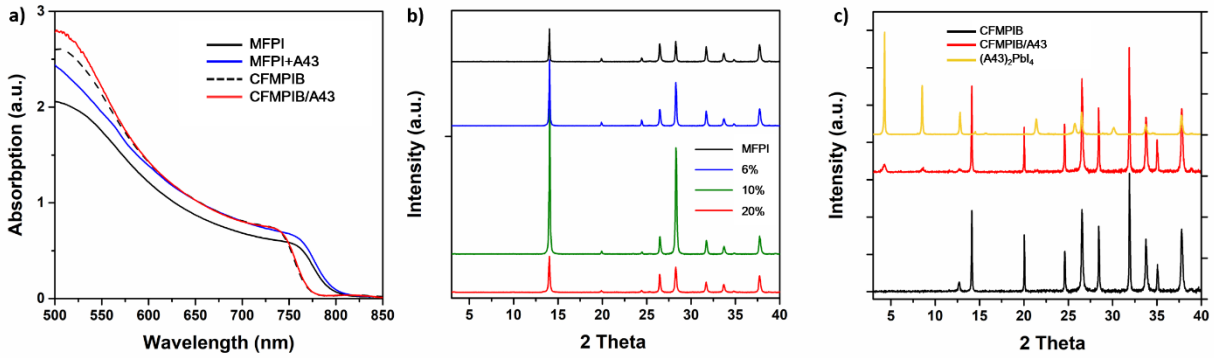
Figure 2. a) UV-Vis absorption spectra of perovskite films as indicated in the legend, where MFPI+A43 indicates the perovskite prepared by the addition of 6% A43 to MFPI precursors, and CFMPIB/A43 indicates the one obtained by the layer-by-layer treatment. b) X-Ray Diffraction (XRD) patterns of MFPI perovskite films containing 0-6-10-20 % A43. c) XRD spectra of pure $(A43)_2PbI_4,$ CFMPIB and CFMPIB/A43.

374
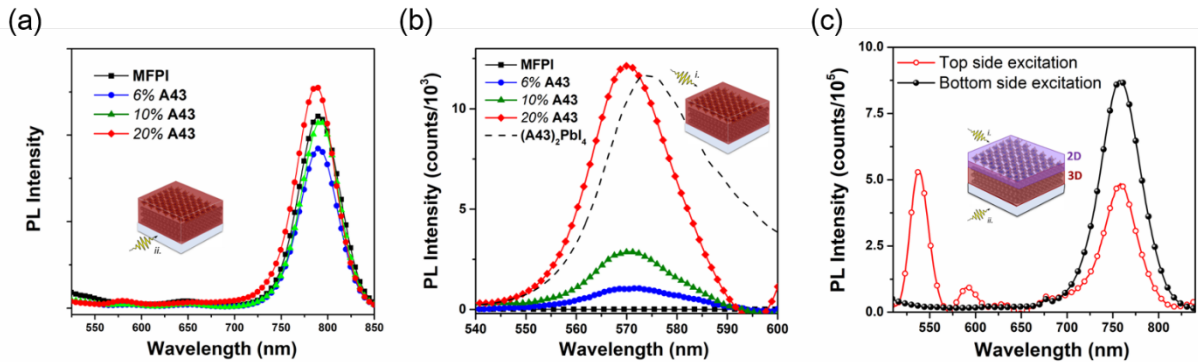
Figure 3. a) Photoluminescence (PL) spectra comparing MFPI and MFPI containing 6-10-20 % A43; PL excitation at 500 nm. b) Micro-PL spectra comparing MFPI and MFPI containing 6-10-20 % A43 in the region around 570 nm. The dashed line represents the PL spectra of the low dimensional perovskite arranging into $(A43)_2PbI_4$ single crystal structure as retrieved from XRD analysis. c) PL spectra of perovskite films CFMPIB/A43 passivated with comparison between top side and bottom side; PL excitation at 420 nm.

18

382
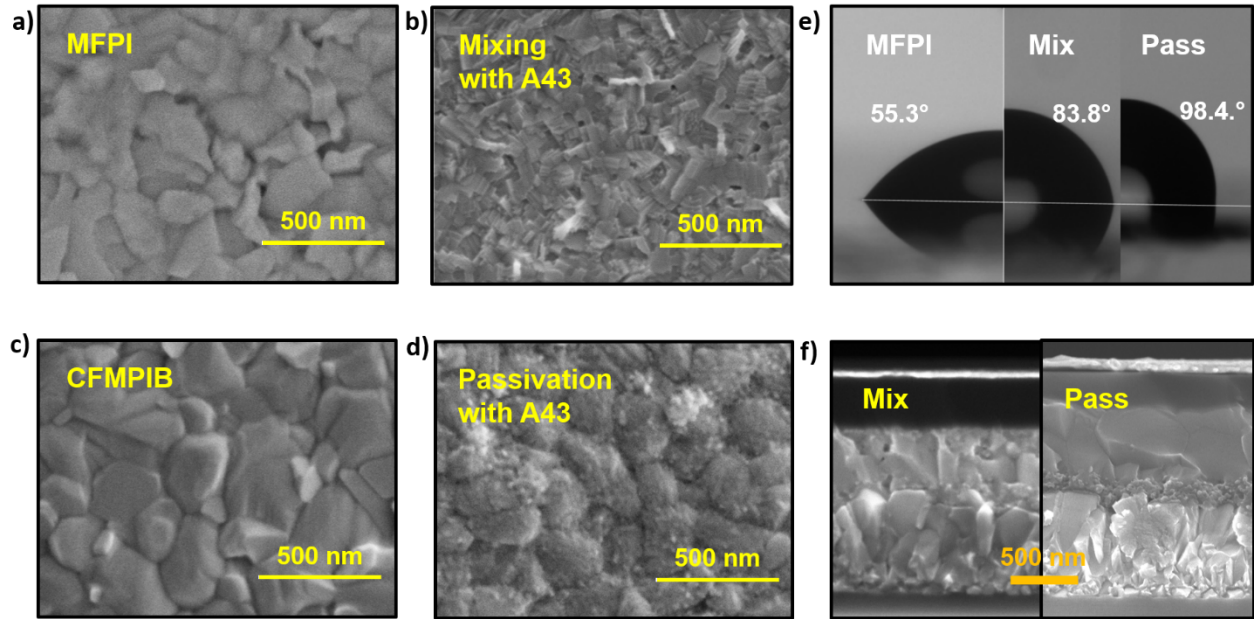
Figure 4. a) and b) Scanning electron microscope (SEM) top view of MFPI and MFPI/ 6% A43; c) and d) SEM images of top-surfaces for CFMPIB and CFMPIB/A43. e) Contact angle images showing a drop of water on top of the pristine MFPI, MFPI containing 6%A43 and the CFMPIB/A43 perovskite films, respectively. f) Cross-sectional SEM images of devices based on MFPI containing 6% A43 and CFMPIB/A43, respectively.
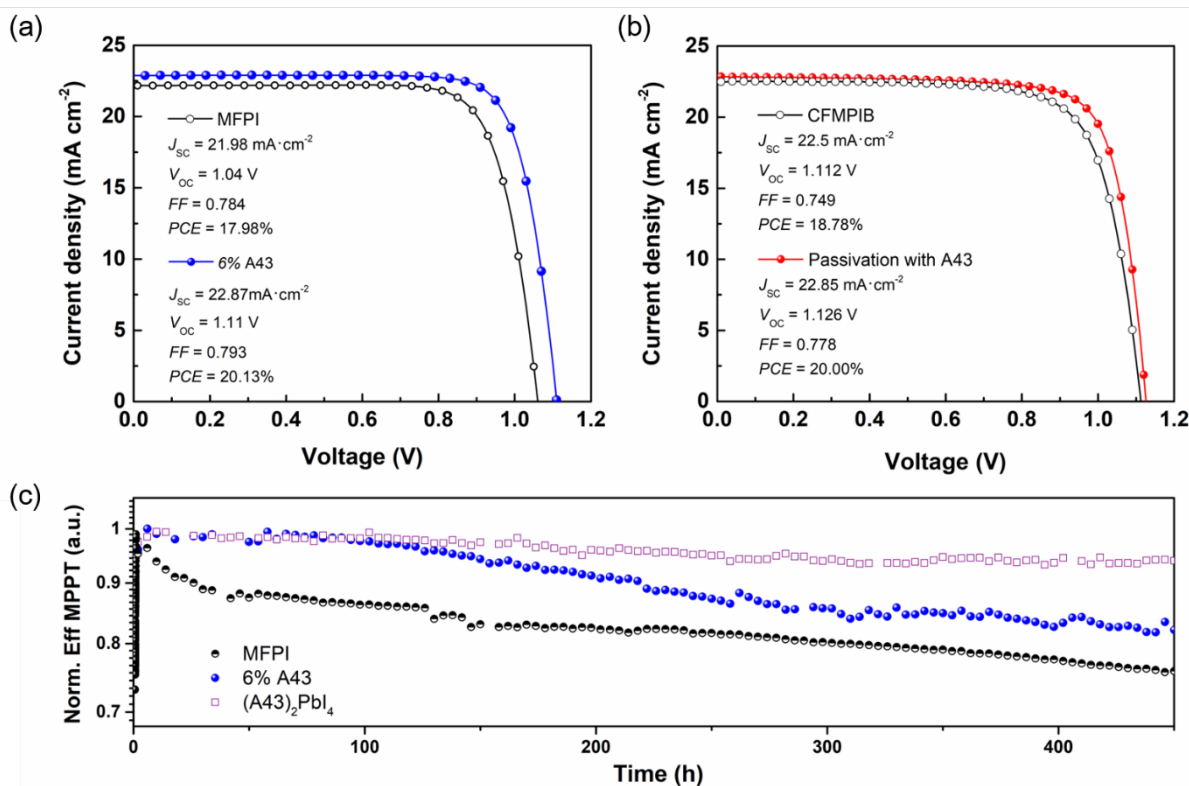
Figure 5. Device characteristic in terms of performances and stability. a) photovoltaic performances of MFPI and MFPI containing 6%A43 solar cells . Device parameters are in the inset. b) J-V curves of CFMPIB and CFMPIB/A43 solar cells. c) Maximum Power point tracking (MPPT) comparing LDP solar cells based on $A43_2PbI_4$, standard 3D MFPI and MFPI containing 6%A43 solar cells.

400 ASSOCIATED CONTENT

401 **Supporting Information**. Additional experimental data are supplied as Supporting Information.

402 **Corresponding Author**

403 *gianluca.pozzi@istm.cnr.it; *giulia.grancini@epfl.ch; *mdkhaja.nazeeruddin@epfl.ch

404 Correspondence should be addressed to giulia.grancini@epfl.ch.

405 **Present Addresses**

406 † School of Chemical Engineering and Technology, Tianjin University, Tianjin 300072, China

407 **Author Contributions**

408 K.T.C. prepared and characterized passivated perovskite cells and revised draft of the

409 manuscript. Z.Y. prepared and characterized mixed perovskite cells; S.O., M.C. and G.P.

410 synthesized new fluorous materials; I.Z. performed the EDX measurements and the single crystal

411 characterization, A. L. performed the contact angle measurements; G.G. designed the

412 experiments, took care of the optical analysis and wrote the first draft of the manuscript; N. T.

413 contributed in the discussion; G.G., G.P. and M.K.N conceived the idea and supervised the

414 research project. All the authors contributed in the data analysis and in the discussion of the

415 manuscript.

422

423   REFERENCES

424

425   (1)   Yang, W. S.; Park, B.-W.; Jung, E. H.; Jeon, N. J.; Kim, Y. C.; Lee, D. U.; Shin, S. S.; Seo,

426   J.; Kim, E. K.; Noh, J. H.; Seok, S. *Science* **2017**, *356* (6345), 1376–1379.

427   (2)   *Http://www.nrel.gov/ncpv/images/efficiency_chart.jpg*.

428   (3)   Green, M. A.; Ho-Baillie, A. *ACS Energy Lett*. **2017**, *2* (4), 822–830.

429   (4)   Grätzel, M. *Acc. Chem. Res*. **2017**, *50* (3), 487–491.

430   (5)   Niu, G.; Guo, X.; Wang, L. *J. Mater. Chem. A* **2015**, *3* (17), 8970–8980.

431   (6)   Wang, D.; Wright, M.; Elumalai, N. K.; Uddin, A. *Sol. Energy Mater. Sol. Cells* **2016**, *147*,

432   255–275.

433   (7)   Domanski, K.; Correa-Baena, J.-P.; Mine, N.; Nazeeruddin, M. K.; Abate, A.; Saliba, M.;

434   Tress, W.; Hagfeldt, A.; Grätzel, M. *ACS Nano* **2016**, *10* (6), 6306–6314.

435   (8)   Saliba, M.; Matsui, T.; Domanski, K.; Seo, J.-Y.; Ummadisingu, A.; Zakeeruddin, S. M.;

436   Correa-Baena, J.-P.; Tress, W. R.; Abate, A.; Hagfeldt, A.; Graetzel, M. *Science* **2016**, *354*

437   (6309), 206–209.

438   (9)   Saliba, M.; Matsui, T.; Seo, J.-Y.; Domanski, K.; Correa-Baena, J.-P.; Nazeeruddin, M. K.;

439   Zakeeruddin, S. M.; Tress, W.; Abate, A.; Hagfeldt, A.; Graetzel, M. *Energy Environ. Sci*.
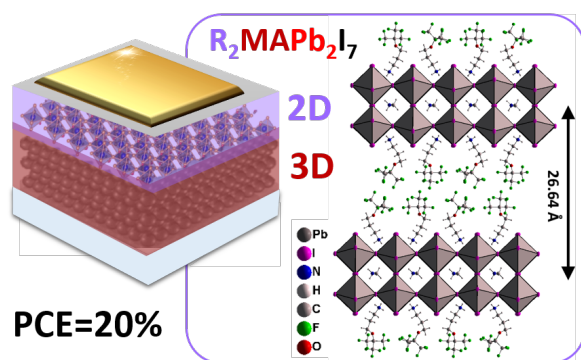
440   **2016**, *9* (6), 1989–1997.

441   (10)   You, J.; Meng, L.; Song, T.-B.; Guo, T.-F.; Yang, Y. (Michael); Chang, W.-H.; Hong, Z.;

442   Chen, H.; Zhou, H.; Chen, Q.; Liu, Y.; De Marco, N.; Yang, Y. *Nat. Nanotechnol.* **2016**, *11*

443   (1), 75–81.

444   (11)   Mei, A.; Li, X.; Liu, L.; Ku, Z.; Liu, T.; Rong, Y.; Xu, M.; Hu, M.; Chen, J.; Yang, Y.;

445   Graetzel, M.; Han, H. *Science* **2014**, *345* (6194), 295–298.

446   (12)   Grancini, G.; Roldán-Carmona, C.; Zimmermann, I.; Mosconi, E.; Lee, X.; Martineau, D.;

447   Narbey, S.; Oswald, F.; Angelis, F. D.; Graetzel, M.; Nazeeruddin, M. K. *Nat. Commun.*

448   **2017**, *8*, ncomms15684.

449   (13)   Zhang, Y.; Grancini, G.; Feng, Y.; Asiri, A. M.; Nazeeruddin, M. K. *ACS Energy Lett.* **2017**,

450   *2* (4), 802–806.

451   (14)   Slavney, A. H.; Smaha, R. W.; Smith, I. C.; Jaffe, A.; Umeyama, D.; Karunadasa, H. I.

452   *Inorg. Chem.* **2017**, *56* (1), 46–55.

453   (15)   Smith, I. C.; Hoke, E. T.; Solis-Ibarra, D.; McGehee, M. D.; Karunadasa, H. I. *Angew.*

454   *Chem. Int. Ed.* **2014**, *53* (42), 11232–11235.

455   (16)   Stoumpos, C. C.; Cao, D. H.; Clark, D. J.; Young, J.; Rondinelli, J. M.; Jang, J. I.; Hupp, J.

456   T.; Kanatzidis, M. G. *Chem. Mater.* **2016**, *28* (8), 2852–2867.

457   (17)   Cao, D. H.; Stoumpos, C. C.; Farha, O. K.; Hupp, J. T.; Kanatzidis, M. G. *J. Am. Chem.*

458   *Soc.* **2015**, *137* (24), 7843–7850.

459   (18)   Mitzi, D. B. In *Progress in Inorganic Chemistry*; Karlin, K. D., Ed.; John Wiley & Sons,

460   Inc., 1999; pp 1–121.

461   (19)   Tsai, H.; Nie, W.; Blancon, J.-C.; Stoumpos, C. C.; Asadpour, R.; Harutyunyan, B.;

462   Neukirch, A. J.; Verduzco, R.; Crochet, J. J.; Tretiak, S.; Pedesseau, L.; Even, J.; Alam,

463   M.A.; Gupta, G.; Lou, J.; Ajayan, P. M.; Bedzyk, M. J.; Kanatzidis, M. G.; Mohite, A. D.

464   *Nature* **2016**, *536* (7616), 312–316.

465 (20) Quan, L. N.; Yuan, M.; Comin, R.; Voznyy, O.; Beauregard, E. M.; Hoogland, S.; Buin, A.;

466   Kirmani, A. R.; Zhao, K.; Amassian, A.; Kim, D. H.; Sargent, E. H. *J. Am. Chem. Soc.*

467   **2016**, *138* (8), 2649–2655.

468 (21) Yao, K.; Wang, X.; Xu, Y.; Li, F. *Nano Energy* **2015**, *18* (Supplement C), 165–175.

469 (22) Yao, K.; Wang, X.; Li, F.; Zhou, L. *Chem. Commun.* **2015**, *51* (84), 15430–15433.

470 (23) Ma, C.; Leng, C.; Ji, Y.; Wei, X.; Sun, K.; Tang, L.; Yang, J.; Luo, W.; Li, C.; Deng, Y.; et

471   al. *Nanoscale* **2016**, *8* (43), 18309–18314.

472 (24) Wang, Z.; Lin, Q.; Chmiel, F. P.; Sakai, N.; Herz, L. M.; Snaith, H. J. *Nat. Energy* **2017**, *2*

473   (9), nenergy2017135.

474 (25) Cho, Y.; Soufiani, A. M.; Yun, J. S.; Kim, J.; Lee, D. S.; Seidel, J.; Deng, X.; Green, M. A.;

475   Huang, S.; Ho-Baillie, A. W. Y. *Adv. Energy Mater.* **2018**, vol (n), 1703392.

476 (26) Koh, T. M.; Shanmugam, V.; Guo, X.; Lim, S. S.; Filonik, O.; Herzig, E. M.; Müller-

477   Buschbaum, P.; Swamy, V.; Chien, S. T.; Mhaisalkar, S. G.; Mathews, N. *J. Mater. Chem.*

478   *A* **2018**, *6* (5), 2122–2128.

479 (27) Zhang, J.; Bai, D.; Jin, Z.; Bian, H.; Wang, K.; Sun, J.; Wang, Q.; Liu, S. (Frank). *Adv.*

480   *Energy Mater.* **2018**, *8* (15), 1703246.

481 (28) Lin, Y.; Bai, Y.; Fang, Y.; Chen, Z.; Yang, S.; Zheng, X.; Tang, S.; Liu, Y.; Zhao, J.; Huang,

482   J. *J. Phys. Chem. Lett.* **2018**.

483 (29) Vincent, J.-M. *Chem. Commun.* **2012**, *48* (93), 11382–11391.

484 (30) Saparov, B.; Mitzi, D. B. *Chem. Rev.* **2016**, *116* (7), 4558–4596.

485 (31) D'Innocenzo, V.; Grancini, G.; Alcocer, M. J.; Kandada, A. R. S.; Stranks, S. D.; Lee, M.

486   M.; Lanzani, G.; Snaith, H. J.; Petrozza, A. *Nat. Commun.* **2014**, *5*.

487 (32) Roldan-Carmona, C.; Gratia, P.; Zimmermann, I.; Grancini, G.; Gao, P.; Graetzel, M.;

488   Nazeeruddin, M. K. *Energy Environ. Sci.* **2015**, *8* (12), 3550–3556.

489 (33) Bi, D.; Gao, P.; Scopelliti, R.; Oveisi E.; Luo J.; Grätzel M.; Hagfeldt A.; Nazeeruddin, M.

490   K. *Adv. Mater.* **2016**, *20*, 2910-2915

491 (34) Bi, E.; Chen, H.; Xie, F.; Wu, Y.; Chen, W.; Su, Y.; Islam, A.; Grätzel, M.; Yang, X.; Han,

492   L. *Nat. Commun.* **2017**, *8*, ncomms15330.

493 (35) deQuilettes, D. W.; Zhang, W.; Burlakov, V. M.; Graham, D. J.; Leijtens, T.; Osherov, A.;

494   Bulović, V.; Snaith, H. J.; Ginger, D. S.; Stranks, S. D. *Nat. Commun.* **2016**, *7*, 11683.

495 (36) De Bastiani, M.; Dell'Erba, G.; Gandini, M.; D'Innocenzo, V.; Neutzner, S.; Kandada, A.

496   R. S.; Grancini, G.; Binda, M.; Prato, M.; Ball, J. M.; Caironi, M.; Petrozza, A. *Adv. Energy*

497   *Mater.* **2016**, *6* (2).

498 (37) Frost, J. M.; Walsh, A. *Acc. Chem. Res.* **2016**, *49* (3), 528–535.

499 (38) Sanehira, E. M.; Tremolet de Villers, B. J.; Schulz, P.; Reese, M. O.; Ferrere, S.; Zhu, K.;

500   Lin, L. Y.; Berry, J. J.; Luther, J. M. *ACS Energy Lett.* **2016**, *1* (1), 38–45.

501 **TOC.**

502